Ion Segregation and Deliquescence of Alkali Halide Nanocrystals on SiO_2

Kenta Arima,[†] Peng Jiang,[‡,§] Deng-Sung Lin,[||] Albert Verdaguer,[⊥] and Miquel Salmeron*[,‡,§]

Department of Precision Science and Technology, Graduate School of Engineering, Osaka University, 2-1, Yamada-oka, Suita, Osaka 565-0871, Japan, Materials Sciences Division, Lawrence Berkeley National Laboratory, Berkeley, California 94720, Department of Materials Science and Engineering, University of California-Berkeley, Berkeley, California 94720, Department of Physics, National Tsing Hua University, 101 Section 2 Kuang Fu Road, Hsinchu 30013, Taiwan, Centre d'Investigació en Nanociència i Nanotecnologia, CIN2 (CSIC-ICN), Campus de la UAB, Edifici CM-7, 08193-Bellaterra, Catalunya, Spain

Received: May 4, 2009; Revised Manuscript Received: July 21, 2009

The adsorption of water on alkali halide (KBr, KCl, KF, NaCl) nanocrystals on SiO_2 and their deliquescence was investigated as a function of relative humidity (RH) from 8% to near saturation by scanning polarization force microscopy. At low humidity, water adsorption solvates ions at the surface of the crystals and increases their mobility. This results in a large increase in the dielectric constant, which is manifested in an increase in the electrostatic force and in an increase in the apparent height of the nanocrystals. Above 58% RH, the diffusion of ions leads to Ostwald ripening, where larger nanocrystals grow at the expense of the smaller ones. At the deliquescence point, droplets were formed. For KBr, KCl, and NaCl, the droplets exhibit a negative surface potential relative to the surrounding region, which is indicative of the preferential segregation of anions to the air/solution interface.

Introduction

In recent years, reactions at the air/aqueous solution interface have attracted a great deal of attention, particularly for alkali halide solutions because of their relevance to atmospheric chemical processes.[1−7] Molecular dynamics[8,9] and Monte Carlo[10] simulations on alkali halide solutions have shown that there is a propensity of the large anions to segregate to the water−air surface. Ex situ atomic force microscopy (AFM) and X-ray photoelectron spectroscopy (XPS) have revealed Br^- segregation in NaBr in NaBr/NaCl crystals grown from aqueous solutions.[11] Second-harmonic-generation spectroscopy,[12,13] vibrational sum-frequency generation spectroscopy,[14−16] and photoionization[17] have also been used to investigate the segregation propensity of various ions. Among the experimental methods, ambient-pressure XPS is particularly useful because it enables quantitative measurements of ionic concentration in the entire relative humidity (RH) range (0−100%) by introducing water vapor and lowering the sample temperature.[18−21] More recently, Ghosal et al. presented a direct measurement of the ion distribution in a mixed NaBr/NaCl aqueous solution.[22] They showed the segregation of Br^- to the solution surface.

Another important in situ method of investigating liquid surfaces is scanning polarization force microscopy (SPFM)[23,24] because it can provide surface topography and surface potential images simultaneously.[25−27] Dai et al.[28] showed the motion of atomic steps on the NaCl surface at humidities above 40%. Luna et al.[29] demonstrated that each alkali halide (NaCl, KCl, KBr, and KI) has a critical RH at which the rate of increase of the surface potential and ionic mobility changes drastically. Recently, the initial stages of water adsorption on NaCl have been studied in detail.[30] Preferential solvation of anions at step edges, followed by solvation of terrace ions, was found. Another experiment on Br-doped NaCl has shown that Br-rich islands segregate to the surface after exposure to RH above 40%, followed by drying, indicating the preferential solvation and segregation of Br^-.[31]

Airborne saline droplets in the troposphere often form around solid particles of dust that originate in deserts and are transported in the atmosphere over long distances to oceanic regions. As a result, a large fraction of the aerosol particles is a mixture of minerals and sea salts.[32−36] Because quartz (SiO_2) is one of the dominant minerals in the dust particles, an investigation of the dissolution and possible ion segregation of salts deposited on quartz or silica substrates can help us to understand the chemical reactions involving aerosols in the troposphere. As the salt dissolves under high humidity, a thin film of the solution will cover the solid substrate, giving rise to two different interfaces, one with the air and the other with the SiO_2 substrate. Because these two interfaces might be separated by short, nanometer scale distances, it can lead to dissolution and segregation mechanisms that are very different from those occurring on pure droplet solutions with a single air/liquid interface.

The purpose of the present study therefore is to investigate the water adsorption and the dissolution of alkali halide crystals on SiO_2 surfaces. In this article, we will present the results obtained by SPFM, and in a subsequent report, now in preparation, we will report spectroscopic results using XPS under ambient conditions.

Experimental Section

Principle of Scanning Polarization Force Microscopy. The operation of SPFM has been previously reported in detail;[26,27] therefore, only a brief description is presented here. SPFM is a noncontact AFM operation mode based on electrostatic forces. When a conductive cantilever is electrically biased (V) relative to a sample or sample support, an attractive electrostatic force

* Corresponding author.
[†] Osaka University.
[‡] Lawrence Berkeley National Laboratory.
[§] University of California-Berkeley.
[||] National Tsing Hua University.
[⊥] Centre d'Investigació en Nanociència i Nanotecnologia.

10.1021/jp904151m CCC: $40.75 © 2009 American Chemical Society
Published on Web 08/11/2009

$F(V)$ acts between tip and sample that can be represented as $F(V) = aV^2 + bV + c$, where a, b, and c are parameters that depend on the geometry of the tip (radius and shape),[37] tip−sample separation, and the local dielectric constants at the sample surface. The first component (aV^2) originates from the polarization of the sample by the biased tip (induced charges). The other components derive from the interaction between the tip and charges or dipoles preexisting on the surface. When a sinusoidal voltage $V = V_{dc} + V_{ac} \sin(\omega t)$, is applied to the cantilever, $F(V)$ has contributions at dc, ω, and 2ω frequencies. The second-harmonic term ($F_{2\omega}$) has information on the polarizability (dielectric constant) and topography, whereas the first-harmonic term ($F_{1\omega}$) represents the electrostatic force induced by the contact potential difference between tip and sample.[38,39] The oscillation of the cantilever is detected by a conventional optical lever technique, and the $F_{2\omega}$ and $F_{1\omega}$ contributions are separated by lock-in amplifiers. A feedback loop controls the tip−sample separation (z) by keeping $F_{2\omega}$ constant. A map of the z displacement represents a surface topography modulated by the local dielectric constant, which will be called "topographic image" for simplicity. A second feedback loop is formed by adding a V_{dc} signal to null $F_{1\omega}$, as in the Kelvin probe method. This gives an image of the local contact potential difference between tip and sample, which we will refer to as a "surface potential image". The surface potential of the tip is unknown during the experiment so that only relative changes in potential between different areas of the surface are meaningful. In addition, because both the tip apex and the larger supporting cantilever contribute to the electrostatic force, the value of the contact potential difference depends on the tip−surface distance. At close proximity (of the order of the tip radius), the contribution of the tip apex is important, whereas at larger separations, the cantilever base is dominant. For these reasons, it can be difficult to perform quantitative measurements of absolute surface potentials.

Sample Preparation. Boron-doped Si(100) wafers with 0.001 Ω·cm resistivity were used as substrates. The wafer was first dipped in a solution of H_2SO_4/H_2O_2 (95−97 and 35 wt %, respectively) = 3:1 (by volume) for 10 min to remove carbon and metallic contamination on the surface. After being rinsed with Millipore water for 1 min, the sample was dipped in a diluted HF solution (1−5%) for 5 min to remove the native oxide.[40] Then, it was treated with an ultraviolet ozone generator for 20 min to form a clean oxide surface. Using XPS, we estimated the oxide thickness to be 2 nm.[41] The sample was exposed to an O_2/Ar plasma at 0.4 Torr for 10 min to generate nucleation sites for the alkali halide crystals. After the plasma treatment, the surface was hydrophilic with a water contact angle smaller than 5°.

For KBr, we used a standard solution (0.1 mol/L, 99.8%) from Riedel-de Haën or solutions prepared from powder (99.9%) from PIKE Technologies. For KCl, KF, and NaCl, the powders used were 99.999 (KCl) and 99.99% (KF) from Sigma-Aldrich and 99.0% (NaCl) from Fisher Scientific. The standard solution or the powders were diluted with Millipore water. Alkali halide crystallites on the SiO_2/Si wafer were prepared by evaporation of films of aqueous solutions spread over the wafer and dried with N_2 gas, as illustrated in Figure 1a. Figure 1b shows contact mode AFM images under dry conditions with two different equivalent amounts of NaCl deposited. The estimated equivalent amount of alkali halide deposited for SPFM observations was 6 to 10 monolayers.

Scanning Polarization Force Microscopy Setup. Our homemade SPFM head was housed inside a glass bell jar and operated with an electronic controller from RHK Technology. The RH was controlled by the introduction of dry or wet N_2 gas obtained by bubbling through Millipore water. All experiments were performed at room temperature (22 ± 1 C°). The RH was measured with a commercial humidity sensor placed ~15 mm from the sample. The humidity variation was ±1% during scans to obtain one image. The absolute RH values have an uncertainty of ±5%. Si cantilevers coated with Cr/Pt from NanoAndMore were used. The resonant frequency and the spring constant were 13 ± 4 kHz and 0.2 N/m, respectively. Before experiments, the cantilevers were exposed to hexadecanethiol vapor for more than 12 h to render them hydrophobic. The peak amplitude, V_{ac}, and frequency of the sinusoidal ac voltage applied to the conductive cantilever were 3.5 V and 4.5−6.0 kHz, respectively, and the Si wafer was connected to the ground. At each RH, topographic and surface potential images were simultaneously obtained. The interval between consecutive images at different RHs was approximately 1 h, to ensure uniformity and stability of the RH in the chamber.

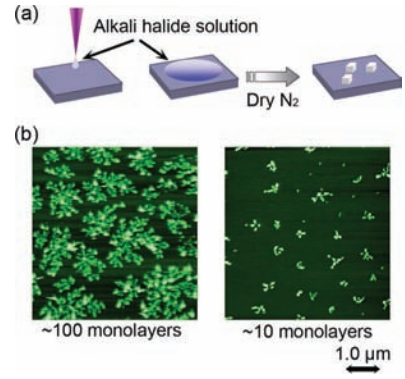

Figure 1. (a) Schematic drawing illustrating the process used for deposition of alkali halide crystallites on SiO_2 from a droplet of solution spread and dried over the wafer surface. (b) Examples of AFM images of NaCl nanocrystals deposited in the manner in part a. They were taken in the contact mode under a dry condition. The 5 × 5 μm^2 images show crystallites in different aggregation states depending on the initial concentration of the solution with heights of roughly 10−20 nm.

Results

Figures 2 and 3 show snapshots of topography (left images) and surface potentials (right images) of KBr crystallites on the Si wafer at different RH. The actual shape of the small salt crystallites cannot be determined from these SPFM noncontact images because of limited lateral resolution, which is determined by tip radius and tip−sample distance, all on the order of a few tens of nanometers. Figure 2 shows results at low humidity (RH < 32%). Bright protrusions in Figure 2a correspond to KBr nanocrystals at 8% RH with heights from 8 to 26 nm. At 8% RH, the surface potential contrast is 9−15 mV positive relative to the surrounding SiO_2 substrate. After the RH is increased to 32%, the crystals remain visible in the topographic image (Figure 2b, left), but the contrast in the surface potential decreases substantially (Figure 2b, right). This trend continues up to 44% RH. Beyond 58% RH, the nanocrystals began to disappear in the topographic images, as shown in Figure 3b−d. First, the small crystals disappear, such as those marked by dotted arrows in Figure 3a. At 86% RH, close to the deliquescence point of bulk KBr, only the larger nanocrystal marked A remains in the imaged area (Figure 3c, left). At 95% RH, none of the crystallite structures can be observed (Figure 3d, left). The lack of contrast is most probably due to the formation of a homogeneous solution film covering the surface. The surface

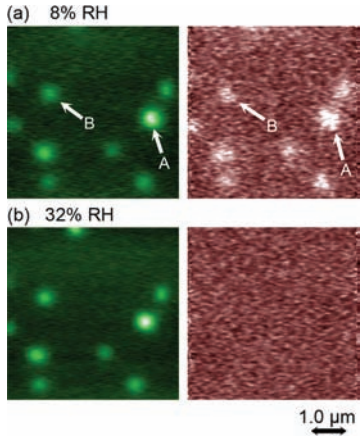

Figure 2. 5×5 μm^2 noncontact SPFM images of KBr nanocrystals on thin SiO_2 films at low relative humidity (RH) of (a) 8 and (b) 32%. Left and right figures are topographic and surface potential images, respectively. Nanocrystal A is ~26 nm high and has a surface potential contrast of ~15 mV. Nanocrystal B is ~13 nm high, and its surface potential is ~10 mV. All nanocrystals show positive contrast in the surface potential image at 8% RH, but this contrast becomes very small when the RH is increased to 32%. For topographic images, the color scales are (a) 26 and (b) 30 nm, respectively. For surface potential images, the color scale is fixed to 20 mV.

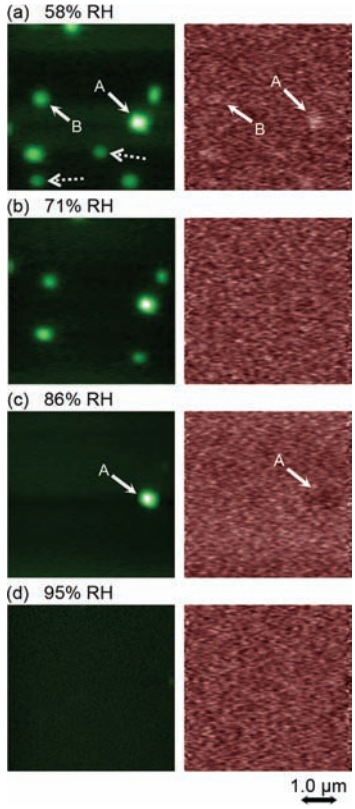

Figure 3. 5×5 μm^2 SPFM images at medium and high relative humidity (RH) of the same area as that in Figure 2. Left and right images correspond to topography and surface potential, respectively. (a) RH = 58%. (b) RH = 71%. The smaller nanocrystals indicated by dotted arrows in part a disappear first. (c) RH = 86%. Only the larger nanocrystal A remains. (d) At RH = 95%, no structures can be observed in either the topographic or the surface potential images. The color scales are (a) 47, (b) 48, (c) 55, and (d) 55 nm, respectively, in the topographic images. For surface potential images, the color scale is fixed to 20 mV.

potential images (Figure 3, right) show a weak negative contrast, down to −7 mV in this RH range.

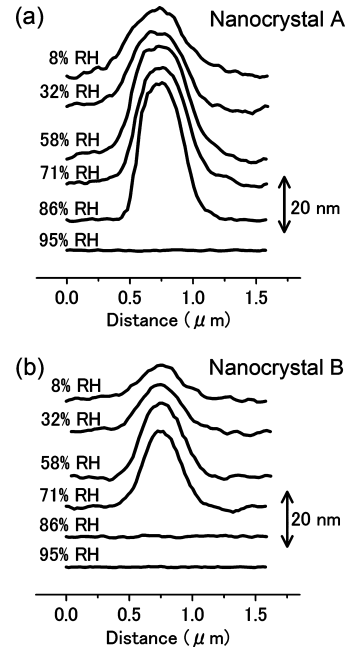

Figure 4. Cross-sectional height profiles of nanocrystals (a) A and (b) B in Figures 2 and 3 as a function of RH. The profiles are shifted vertically for clarity.

Figure 4 shows cross-sectional profiles of crystals labeled A and B in Figures 2 and 3. In Figure 4a, the initial apparent height of nanocrystal A is ~26 nm at 8% RH and increases with RH to reach a maximum of ~53 nm at 86% RH. At 95% RH, it becomes completely flat, which indicates dissolution. Nanocrystal B is ~13 nm high under dry conditions (8% RH) and also grows in apparent height as the RH increases, reaching ~28 nm at 71% RH. Interestingly, it flattens out at lower RH (between 71 and 86%) than nanocrystal A.

In another experiment, a KBr nanocrystal ~29 nm high under dry conditions (8% RH) was exposed to water vapor, and its apparent height increased to ~78 nm at 72% RH. After drying again to 8% RH, the apparent height was found to be ~60 nm. This example indicates that the physical size of the KBr nanocrystals increased, most likely because of accretion of ions that diffused away from the smaller particles at high humidity, as we discuss in more detail later.

Figure 5 shows another SPFM result at high RH close to the deliquescence point. Left and right figures are topographic and surface potential images, respectively. Figure 5a shows 4×4 μm^2 images taken at 67% RH of four KBr nanocrystals (labeled C, D, E, and F) with heights of ~20, ~12, ~15, and ~15 nm, respectively. No contrast can be seen in the surface potential image (Figure 5a, right). Figure 5b shows images taken at 81% RH. Nanocrystals E and F in Figure 5a disappear. Nanocrystal C gives rise to a small negative contrast (−3 mV) in the surface potential image, whereas that of nanocrystal D is within the noise (Figure 5b, right). The images in Figure 5c, 7×7 μm^2, were taken at 95% RH. The nanocrystals (C and D) have dissolved completely, producing a large flat droplet or film (Figure 5c, left). The surface potential of the film is negative relative to that of the surrounding area (Figure 5c, right). The area in Figure 5b is contained inside the area occupied by the film in Figure 5c. Figure 6a shows cross-sectional profiles of the nanocrystal labeled C in Figures 5a,b. The apparent height of nanocrystal C increases from ~20 to ~27 nm by the increase in RH from 67 to 81%. Nanocrystal D also increased its height from ~12 to ~17 nm. Figure 6b shows topographic and surface

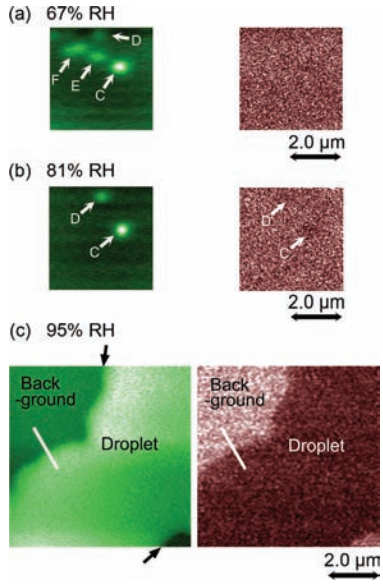

Figure 5. Noncontact SPFM images of KBr nanocrystals on thin SiO_2 films at a relative humidity (RH) near the deliquescence point. Left and right figures are topographic and surface potential images, respectively. (a) RH = 67%. The contrast range in the topographic image is 25 nm. Four nanocrystals marked C, D, E, and F are visible in the 4 × 4 μm^2 area. No contrast can be seen in the surface potential image. (b) RH = 81%. Only two nanocrystals marked C and D are visible in the 4 × 4 μm^2 area. The contrast range is 33 nm (left) and 12 mV (right). (c) RH = 95%. The scanned area is 7 × 7 μm^2 and includes the regions of the images in part b. At this RH, the nanocrystals have dissolved completely, forming a flat droplet of the solution. Arrows indicate the boundaries of the droplet. The color scales are 13 nm (left) and 20 mV (right).

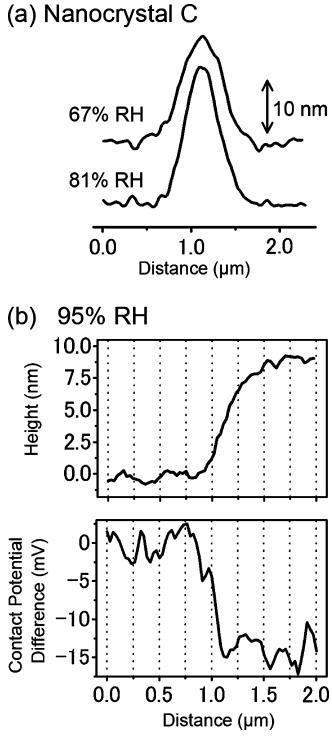

Figure 6. (a) Cross-sectional height profiles of nanocrystal C in Figure 5a,b. The profiles are shifted vertically for clarity. (b) Cross-sectional cuts along white lines in Figure 5c.

potential profiles across white lines in Figure 5c. The film is ~9 nm high and approximately −15 mV more negative than the surrounding area.

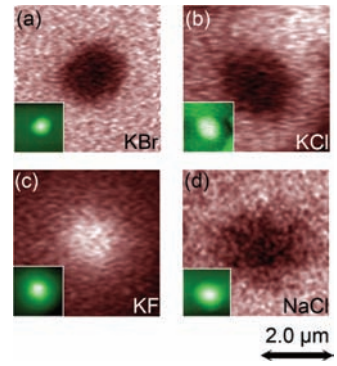

Figure 7. Surface potential images of several deliquesced alkali halides on SiO_2. The scanned area is 4 × 4 μm^2 in all images. A topographic image of each droplet is shown as an inset in the lower left corner. (a) KBr, (b) KCl, (c) KF, and (d) NaCl. Images were taken at high relative humidity (RH) ((a) RH = 93%, (b) RH = 92%, (c) RH = 90%, (d) RH = 95%). The color scales are (a) 25, (b) 25, (c) 35, and (d) 25 mV.

We attribute the negative contrast of the surface potential over the areas occupied by the dissolved salt crystals to the preferential segregation of the anions to the solution/air interface. Recent simulations[8−10] and experiments[11−17,21,22] have indeed shown an enhancement of concentration of the larger, more polarizable halogen ions at the surface of aqueous solutions. Our results imply that this phenomenon also occurs in nanometer-thick solution films, which is now limited by two interfaces, the air/liquid and the liquid/SiO_2. This result is relevant to atmospheric chemistry because most droplets are presumably formed around solid nuclei, like silica sand particles.

To explore the dependence of the segregation trends on anion size, we performed experiments with various alkali halides, including KBr, KCl, KF, and NaCl with deliquescence points of ~86, ~87, ~25, and ~75% RH, respectively.[29] Figure 7 shows 4 × 4 μm^2 surface potential images of droplets formed by deliquescence of these alkali halide particles at RH higher than 90%. A topographic image of each droplet is shown in the inset. The surface potential is negative relative to the surrounding area for KBr, KCl, and NaCl but positive for KF. The values of the potential over the KBr, KCl, KF, and NaCl droplets are -18 ± 3, -14 ± 2, $+25 \pm 5$, and -10 ± 3 mV, respectively. These results are in line with the segregation of Br^- and Cl^- ions to droplet surfaces, the effect being stronger with Br^- than with Cl^- ions. The smaller F^- ions are depleted at the air/droplet interface. Unfortunately, the dependence of the contact potential with tip−surface distance prevents a determination of the degree of ion segregation from the measured values of the contact potential.

Discussion

The decrease in contrast of the surface potential with increasing RH from 8 to 32% in Figure 2 indicates that the adsorption of water on the KBr nanocrystals and the SiO_2 surface smoothes out the initial difference of surface potentials formed under dry conditions. The apparent height, however, increases as a function of humidity until the deliquescence point is reached, at which point it collapses, as shown in Figure 4 for KBr. To understand this increase, let's consider the various possible contributions to the contrast. The first one is physical and reflects the growth of KBr. A second one could be a preferential adsorption of water on the crystallites over the surrounding SiO_2. Both contributions give rise to topographic changes that reflect a real increase in the amount of material in

the crystallite or droplet. The third one is due to an increase in dielectric constant, which leads to higher electrostatic forces.

As alkali halide crystal surfaces are exposed to water, ions solvate and become mobile, leading to an increase in the local dielectric constant, ε. This starts first at step edges and is reflected in an enhanced step contrast.[30] The increase in attractive electrostatic force due to the changes in the dielectric constant eventually saturates because the electrostatic force increases following a relation of the type $(\varepsilon - 1)/\varepsilon$.[24,26,42] Because we know from ambient-pressure XPS that the amount of water on KBr thin films on SiO_2 is no more than a few monolayers thick around 55% RH,[43] we believe that the observed increase in apparent height up to ~58% RH in Figure 4 is mostly of dielectric origin.

The small crystallites other than nanocrystal A in Figure 3a and nanocrystals E and F in Figure 5a disappear in the humidity range between 58 and 86% RH. One may think that smaller nanocrystals deliquesce at lower RH. This is not likely in this case, however, because droplets such as those in Figures 5c and 7 have never been observed in this humidity range. The most likely explanation is the occurrence of Ostwald ripening in which the increase in the number and mobility of solvated ions as the humidity continues to increase beyond 55% RH results in an enhanced ionic diffusion that transports ions from the small to the larger crystallites. The increase in apparent heights of large nanocrystals is clearly visible for nanocrystal A (from 71 to 86% RH in Figure 4a) and nanocrystal C (from 67 to 81% in Figure 6a) above ~55% RH. Ostwald ripening has been observed in many physical and chemical systems.[44−46] It is the coarsening of an ensemble of differently sized clusters as larger clusters grow at the expense of smaller ones. The driving force for ripening is the minimization of the total surface area of the cluster ensemble. Recently, Cleaver et al.[47] have found on the surface of boric acid that it undergoes restructuring when exposed to changes in RH of the surrounding air. Their AFM observations, in contact mode, showed the preferential dissolution of submicrometer surface features and the growth of flatter regions at high RH of 80%. Although the thickness of adsorbed water layers is unknown in their study, they proposed that the concept of Ostwald ripening can be extended to account for the dissolution and redistribution of fine surface features or roughness in contact with water layers. Their result supports the Ostwald ripening scenario to explain the contrast increase in the large crystals and the disappearance of small ones in Figures 3 and 5 in the presence of water layers.

One may notice that the apparent heights of nanocrystals A and B do not increase significantly from 58 to 71% RH in Figure 4 despite the disappearance of the two nanocrystals marked by dotted arrows in Figure 3a. The apparent height represents surface topography modulated by the local dielectric constant. The dielectric constant increases because at higher RH because more water is available to solvate and increase the mobility of ions.[30] Because the amplitude of the lever oscillation in SPFM imaging is maintained constant in a topographic image, the tip is being raised over the surface to compensate for the increased force. The larger tip−sample separation results in a lower corrugation because of the decreased spatial variation in electrostatic forces. The apparent heights of the nanocrystals in Figure 4 do not change from 58 to 71% RH, even if the tip−sample separation is increasing. This clearly indicates that the nanocrystals must be growing in this RH range.

In Figure 5b, nanocrystal D is still visible, whereas the larger crystals E and F in Figure 5a have disappeared. The explanation we believe is that solvated ions are exchanged between KBr clusters through the water layers on the SiO_2, which we cannot image.

In our measurements, the size increase in the nanocrystals is apparent mostly in the vertical direction. As explained above, this is related to the limited lateral resolution of SPFM, from both the finite tip apex radius and the large tip−sample separation, on the order of 20−30 nm.[27] One might expect that the aspect ratio (height/width) should be close to 1.0 for cubic nanocrystals. However, the aspect ratio of nanocrystals A and B under dry conditions is much lower than 1.0 in Figure 4, even if we take into account the limited lateral resolution of SPFM. Figure 1b shows images of alkali halide crystallites in the contact mode. Although we cannot resolve the cubic shape, the small crystallites form 2D aggregates. If each aggregate is unresolved and imaged as one protrusion in the SPFM mode, then the aspect ratio of the protrusion would be much smaller than 1.0.

The boundaries of the deliquesced droplet in Figure 5c, marked by arrows, have irregular shapes. In contrast, all droplets in Figure 7 have circular boundaries. The difference in the shape of deliquesced droplets is probably due to the presence and distribution of some contaminant materials such as hydrocarbons on the SiO_2 surface, which are difficult to control completely under our ambient conditions.

Conclusions

We have studied the effect of water adsorption on small crystals of alkali halide deposited on thin SiO_2 films as a function of RH, with the objective of determining the ionic solvation processes leading to crystal dissolution (deliquescence) and the occurrence of preferential cation or anion segregation to the air/liquid and liquid/solid interfaces. Our motivation was to determine if the anion segregation experimentally observed and theoretically predicted at the air−liquid interface also occurs when another interface is present within a few nanometers of the first one. This would be of relevance to atmospheric phenomena involving water condensation on saline deposits on sand grains and other minerals.

First, we focused on KBr nanocrystals and imaged them as a function of RH from 8 to 95%. Up to ~55% RH, water adsorbs and solvates ions, which become mobile and cause an increase in the dielectric constant. This is manifested in a large increase in electrostatic force that produces an increase in the apparent height of the salt crystals. Between approximately 55 and 85% RH, there is a rapid increase in the crystal height because of Ostwald ripening, where large crystals grow at the expense of small ones. At the deliquescence point, the crystals completely dissolve, giving rise to droplets or films. The RH at the deliquescence point of KBr crystallites on SiO_2 is found to be between 86 and 95% RH, virtually identical to that of the bulk KBr crystal (~86% RH).

We also imaged deliquesced droplets of various alkali halides (KBr, KCl, KF, and NaCl). The surface potential of the dissolved salt crystals was found to be negative relative to the surrounding SiO_2 surface except for KF, where the surface potential of the solution was positive. These results support the model of segregation of large anions to the air/liquid interface, even in the presence of a liquid/solid interface located a few nanometers away.

Acknowledgment. This work was supported by the Director, Office of Science, Office of Basic Energy Sciences, Materials Sciences and Engineering Division of the U.S. Department of

Energy under contract no. DE-AC02-05CH11231. K.A. acknowledges financial support from the Yamada Science Foundation. A.V. acknowledges support from the Spanish Ramón y Cajal Program. We thank E. Wong for his technical support on SPFM.

References and Notes

(1) Barrie, L. A.; Bottenheim, J. W.; Schnell, R. C.; Crutzen, P. J.; Rasmussen, R. A. *Nature* **1988**, *334*, 138.
(2) Finlayson-Pitts, B. J.; Livingston, F. E.; Berko, H. N. *Nature* **1990**, *343*, 622.
(3) McConnell, J. C.; Henderson, G. S.; Barrie, L.; Bottenheim, J.; Niki, H.; Langford, C. H.; Templeton, E. M. J. *Nature* **1992**, *355*, 150.
(4) Impey, G. A.; Shepson, P. B.; Hastie, D. R.; Barrie, L. A.; Anlauf, K. G. *J. Geophys. Res. D* **1997**, *102*, 16005.
(5) Impey, G. A.; Mihele, C. M.; Anlauf, K. G.; Barrie, L. A.; Hastie, D. R.; Shepson, P. B. *J. Atmos. Chem.* **1999**, *34*, 21.
(6) Foster, K. L.; Plastridge, R. A.; Bottenheim, J. W.; Shepson, P. B.; Finlayson-Pitts, B. J.; Spicer, C. W. *Science* **2001**, *291*, 471.
(7) Thomas, J. L.; Jimenez-Aranda, A.; Finlayson-Pitts, B. J.; Dabdub, D. *J. Phys. Chem. A* **2006**, *110*, 1859.
(8) Jungwirth, P.; Tobias, D. J. *J. Phys. Chem. B* **2001**, *105*, 10468.
(9) Jungwirth, P.; Tobias, D. J. *J. Phys. Chem. B* **2002**, *106*, 6361.
(10) Eggimann, B. L.; Siepmann, J. I. *J. Phys. Chem. C* **2008**, *112*, 210.
(11) Zangmeister, C. D.; Turner, J. A.; Pemberton, J. E. *Geophys. Res. Lett.* **2001**, *28*, 995.
(12) Petersen, P. B.; Saykally, R. J. *J. Phys. Chem. B* **2006**, *110*, 14060.
(13) Petersen, P. B.; Saykally, R. J. *Annu. Rev. Phys. Chem.* **2006**, *57*, 333.
(14) Liu, D.; Ma, G.; Levering, L. M.; Allen, H. C. *J. Phys. Chem. B* **2004**, *108*, 2252.
(15) Mucha, M.; Frigato, T.; Levering, L. M.; Allen, H. C.; Tobias, D. J.; Dang, L. X.; Jungwirth, P. *J. Phys. Chem. B* **2005**, *109*, 7617.
(16) Ishiyama, T.; Morita, A. *J. Phys. Chem. C* **2007**, *111*, 738.
(17) Grieves, G. A.; Petrik, N.; Herring-Captain, J.; Olanrewaju, B.; Aleksandrov, A.; Tonkyn, R. G.; Barlow, S. A.; Kimmel, G. A.; Orlando, T. M. *J. Phys. Chem. C* **2008**, *112*, 8359.
(18) Ogletree, D. F.; Bluhm, H.; Lebedev, G.; Fadley, C. S.; Hussain, Z.; Salmeron, M. *Rev. Sci. Instrum.* **2002**, *73*, 3872.
(19) Verdaguer, A.; Weis, C.; Oncins, G.; Ketteler, G.; Bluhm, H.; Salmeron, M. *Langmuir* **2007**, *23*, 9699.
(20) Salmeron, M.; Schlögl, R. *Surf. Sci. Rep.* **2008**, *63*, 169.
(21) Ghosal, S.; Hemminger, J. C.; Bluhm, H.; Mun, B. S.; Hebenstreit, E. L. D.; Ketteler, G.; Ogletree, D. F.; Requejo, F. G.; Salmeron, M. *Science* **2005**, *307*, 563.
(22) Ghosal, S.; Brown, M. A.; Bluhm, H.; Krisch, M. J.; Salmeron, M.; Jungwirth, P.; Hemminger, J. C. *J. Phys. Chem. A* **2008**, *112*, 12378.
(23) Hu, J.; Xiao, X.-D.; Ogletree, D. F.; Salmeron, M. *Science* **1995**, *268*, 267.
(24) Hu, J.; Xiao, X.-D.; Salmeron, M. *Appl. Phys. Lett.* **1995**, *67*, 476.
(25) Salmeron, M.; Xu, L.; Hu, J.; Dai, Q. *MRS Bull.* **1997**, *8*, 36.
(26) Xu, L.; Salmeron, M. Chapter 6. In *Nano-Surface Chemistry*; Rosoff, M., Ed.; Marcel Dekker: New York, 2001.
(27) Verdaguer, A.; Sacha, G. M.; Bluhm, H.; Salmeron, M. *Chem. Rev.* **2006**, *106*, 1478.
(28) Dai, Q.; Hu, J.; Salmeron, M. *J. Phys. Chem. B* **1997**, *101*, 1994.
(29) Luna, M.; Rieutord, F.; Melman, N. A.; Dai, Q.; Salmeron, M. *J. Phys. Chem. A* **1998**, *102*, 6793.
(30) Verdaguer, A.; Sacha, G. M.; Luna, M.; Ogletree, D. F.; Salmeron, M. *J. Chem. Phys.* **2005**, *123*, 124703.
(31) Ghosal, S.; Verdaguer, A.; Hemminger, J. C.; Salmeron, M. *J. Phys. Chem. A* **2005**, *109*, 4744.
(32) Andreae, M. O.; Charlson, R. J.; Bruynseels, F.; Storms, H.; Van Grieken, R.; Maenhaut, W. *Science* **1986**, *232*, 1620.
(33) Levin, Z.; Teller, A.; Ganor, E.; Yin, Y. *J. Geophys. Res. D* **2005**, *110*, D20202.
(34) VanCuren, R. A. *J. Geophys. Res. D* **2003**, *108*, 4623.
(35) Fan, X.-B.; Okada, K.; Niimura, N.; Kai, K.; Arao, K.; Shi, G.-Y.; Qin, Y.; Mitsuta, Y. *Atmos. Environ.* **1996**, *30*, 347.
(36) Zhang, D.; Iwasaka, Y. *Geophys. Res. Lett.* **2004**, *31*, L15102.
(37) Gómez-Moñivas, S.; Froufe-Pérez, L. S.; Caamaño, A. J.; Sáenz, J. J. *Appl. Phys. Lett.* **2001**, *79*, 4048.
(38) Schönenberger, C.; Alvarado, S. F. *Phys. Rev. Lett.* **1990**, *65*, 3162.
(39) Yokoyama, H.; Inoue, T. *Thin Solid Films* **1994**, *242*, 33.
(40) Arima, K.; Endo, K.; Kataoka, T.; Oshikane, Y.; Inoue, H.; Mori, Y. *Appl. Phys. Lett.* **2000**, *76*, 463.
(41) Himpsel, F. J.; McFeely, F. R.; Taleb-Ibrahimi, A.; Yarmoff, J. A. *Phys. Rev. B* **1988**, *38*, 6084.
(42) Gómez-Moñivas, S.; Sáenz, J. J.; Carminati, R.; Greffet, J. J. *Appl. Phys. Lett.* **2000**, *76*, 2955.
(43) Arima, K.; Salmeron M., in preparation.
(44) Lifshitz, I. M.; Slyozov, V. V. *J. Phys. Chem. Solids* **1961**, *19*, 35.
(45) Chakraverty, B. K. *J. Phys. Chem. Solids* **1967**, *28*, 2401.
(46) Morgenstern, K.; Rosenfield, G.; Comsa, G. *Phys. Rev. Lett.* **1996**, *76*, 2113.
(47) Cleaver, J. A. S.; Wong, P. *Surf. Interface Anal.* **2004**, *36*, 1592.

JP904151M